Quantifying methane vibrational and rotational temperature with Raman scattering

T.D. Butterworth[1], B. Amyay[2], D. v.d. Bekerom[1], A. v.d. Steeg[1], T. Minea[1], N. Gatti[1], Q. Ong[1], C. Richard[2], C. van Kruijsdijk[3], J.T. Smits[3], A.P. van Bavel[3], V. Boudon[2], & G. J. van Rooij[1].

1 – Dutch Institute for Fundamental Energy Research (DIFFER), De Zaale 20, Eindhoven, 5612 AJ, Netherlands.
2 - Laboratoire Interdisciplinaire Carnot de Bourgogne, UMR 6303 CNRS-Univ. Bourgogne Franche-Comté, 9 Avenue Alain Savary, BP 47 870, F-21078 Dijon Cedex France.
3 – Shell Global Solutions International B.V., Grasweg 31, 1031 HW Amsterdam, Netherlands.

Abstract

This work describes the theoretical basis and implementation of the measurement of vibrational (T_{vib}) and rotational (T_{rot}) temperatures in CH_4 by fitting spontaneous Raman scattering spectra in the Pentad region. This method could be applied for thermal equilibrium temperature measurements applications, e.g. in combustion, or vibrational-rotational non-equilibrium applications, such as in plasma chemistry.

The method of calculating these temperatures is validated against known temperature thermal equilibrium spectra up to 860K from published data, giving an estimated relative error of 10%. This demonstrates that both the calculated stick spectrum and the algorithm to determine T_{vib} and T_{rot} for CH_4 is robust to 860 K, but we expect it is valid to 1500 K. Additionally, a number of non-equilibrium spectra generated with a pulsed microwave plasma are fitted to find T_{vib} and T_{rot}, further demonstrating the applicability of this method in fitting non-equilibrium spectra.

1. Introduction

Raman scattering is a powerful diagnostic technique for measuring gas temperatures and chemical compositions. The Raman spectrum of methane in the pentad region (~3000 cm^{-1}) contains spectral information that can be used to reveal both the vibrational and rotational temperature. Direct temperature measurement from the methane Raman spectrum is challenging due to the complexity of the spectral features, owing to the molecule having 4 coupled fundamental vibrational modes. Despite this difficulty, the ability to directly measure temperature from these spectral features can be critical where it is not an option to perturb the gas, either directly, i.e. with a physical probe, or indirectly. Indirect temperature measurement could be achieved by fitting the Raman spectrum of a diatomic probe molecule, such as N_2 or O_2, where fitting the spectrum to obtain temperatures in equilibrium or non-equilibrium conditions has been implemented with spontaneous Raman [1,2] and CARS [3]. However, probe molecules could play an undesired role in the underlying physics and chemistry of a process, hence, non-disruptive temperature measurement techniques are required in combustion and plasma chemistry. Recent interest in non-equilibrium chemical conversion of molecular gases [4–9] has driven an interest in diagnostics that are able to probe vibrational and rotational population densities of gases with complex Raman spectra, such as CO_2 [10,11]. For this work, we define non-equilibrium for molecular gases as a condition in which the vibrational temperature is in excess of the both the rotational and translational temperature (T_{trans}), where we assume $T_{trans} = T_{rot}$. I.e. there is a significant population of molecules at a vibrational level higher than that predicted by equilibrium thermodynamics based on their translational temperature.

Vibrational excitation of molecules is identified to facilitate dissociation of thermodynamically stable molecules at relatively low translational temperatures [12]. This motivates research into fertiliser production from N_2 that can compete with the Haber-Bosch process [8,13], CO_2 conversion to "solar fuels" to help provide economic drivers to mitigate climate change [7], and in the case of CH_4, the potential for selective conversion [14,15] to important commodity hydrocarbons such as ethylene (C_2H_4).

In order to generate strong vibrational-rotational non-equilibrium conditions we use a pulsed low pressure microwave generated plasma. This non-equilibrium is also observed using CO_2 in [16]. The electric field of the incident microwave accelerates free electrons, which leads to further ionisation and the ignition of a plasma. Due to their low reduced electric fields, microwave generated plasmas are characterised by a relatively high population density of low energy electrons (electron temperatures around 1-2eV). At electron temperatures of 1-2 eV, electron impact cross sections for vibrational excitation are at a maximum, meaning that electron energy will be selectively transferred to vibrational modes of molecules.

Vibrational energy can be transferred between molecules, leading to population of higher vibrational levels through vibrational-vibrational (VV) excitation, or relaxation to translational energy (i.e. heat) through vibrational-translational (VT) relaxation [17–19]. Gas heating can also be caused by various other mechanisms, such as direct electron impact dissociation, electron-ion dissociative recombination, or collisional quenching of electronically excited states. As gas temperature increases the rate of VT relaxation also increases, ultimately leading to equilibration of the vibrational and translational energies. In this way, a non-equilibrium between T_{vib} and $T_{rot/trans}$ can be established for timescales on the order of gas heating mechanisms in the plasma.

In order to assess the extent of non-equilibrium, it is useful to be able to measure both T_{vib} and T_{rot} (T_{rot} is assumed to be equal to T_{trans} due to fast energy redistribution [20]) by fitting the Raman spectrum in one spectral region. Experimentally, this requires a strong signal intensity, sensitivity across a broad temperature range, and spectral peaks that can be sufficiently resolved. Furthermore, simulation of the spectrum requires the ability to calculate positions and intensities of spectral lines. This is relatively straightforward in the case of diatomic molecules, where line data can be calculated from spectroscopic constants (N.B. they may also be derived from ab-initio calculation and Hamiltonian methods). However, in the case of case of more complex molecules, such as CH_4, spectral data is required to be calculated via an effective Hamiltonian method, described in section 3.

The complexity of the methane Raman spectrum originates from its 4 fundamental vibrational modes that are coupled through anharmonic and Coriolis interactions [21,22]. A summary of properties is shown in Table 1. The interaction between these vibrational modes leads to well defined spectral bands, termed polyads. The first of these polyads is the Dyad, formed at around 1500 cm^{-1} which is composed of single quantum Raman transitions of the 2 bending modes, v_2 and v_4. It potentially provides a great deal of information due to the presence of both a Q branch ($\Delta J = 0$) and P,O, R and S branches ($\Delta J = -2, -1, +1, +2$, respectively), that are particularly beneficial in determining rotational temperatures. Despite this, we do not consider the dyad in this work due to the low signal intensity of the band in spontaneous Raman scattering.

The second polyad is the Pentad, occurring around the 3000 cm^{-1} region. The pentad takes its name from the 5 possible Raman transitions that can occur in this region, that is: v_1, v_3, $2v_2$, $2v_4$, $v_2 + v_4$. In this region the symmetric stretch mode (v_1) has the highest Raman cross section, giving it sufficient intensity to be easily measured over a wide range of temperatures. With increasing temperatures "hot bands" form due to higher vibrational levels being populated, differing from the band centre due to anharmonicity. With a sufficiently high resolution spectrometer, the peaks of the hot bands can be well resolved in order to fit both T_{vib} and T_{rot}. From the relative heights of these different peaks it is possible to calculate different vibrational population densities. Similarly, rotational population densities can be determined by the peak shape, where increasing rotational temperature leads to an asymmetric broadening of the peak. The selection rule for rotational transitions for the v_1 vibrational transition is $\Delta J = 0$, so only Q-branches are observed. Hence, the spectral region around the v_1 and its hot-bands can be fitted with T_{vib} and T_{rot} as free parameters.

This paper describes the method used to calculate the line spectrum at different vibrational and rotational temperatures. Subsequently, these fits are demonstrated to yield reliable temperature information for equilibrium conditions on the basis of reference spectra from literature. Finally, we apply the spectral fitting routine to measure both the vibrational and rotational temperature in microwave plasma generated non-equilibrium conditions.

2. Theory - Calculation of the methane Raman spectrum

2.1 Calculation of the stick spectrum

The Raman spectra of methane are calculated in this work using the STDS software developed in Dijon [23] which is based on a vibration-rotation effective Hamiltonian suitable for calculating the energy levels of spherical type molecules. As for energies, an effective polarizability tensor is used for Raman intensities. The characteristics of this effective model are described below.

The Pentad system, specifically the v_1 band around 2932 cm^{-1} is the focus of this calculation. Calculations were performed in te thermodynamic equilibrium conditions, so that $T_{vib} = T_{rot} \approx 1500K$. In addition to the cold bands, a series of hot bands with $\Delta_n = \pm 1$, and ± 2 (n being the polyad number), were calculated up to and including the Tetradecad, P4. All of these bands were calculated rotationally up to J = 30.

2.2 The effective Hamiltonian

The conventional normal modes of methane ($^{12}CH_4$) are respectively: the v_1 mode, a nondegenerate symmetric CH stretching vibration with symmetry A_1, the v_2 mode, a doubly degenerate CH bending vibration with symmetry E and two triply degenerate modes with symmetry F_2, the v_3 being a CH stretching vibration and the v_4 mode corresponding to a CH bending vibration. Their corresponding frequencies exhibit an approximate relation between stretching and bending modes ($v_1 \approx v_3 \approx 2v_2 \approx 2v_4$), see Table 1.

Table 1: The vibrational normal modes frequency of $^{12}CH_4$ obtained from the global analysis published in [24]. The numbers between parentheses are the uncertainties, in the units of the last digits quoted. The zero-point-energy (ZPE) is calculated using the following expression: $ZPE \ (cm^{-1}) = \sum_s hcv_s \frac{d_s}{2}$; where h and c are the Planck constant and speed of light, respectively.

$^{12}CH_4$ vib. Modes	Symmetry	Degeneracy (d_s)	Frequency (cm^{-1})
v_1	A_1	1	2932.369(31)
v_2	E	2	1533.332567(26)
v_3	F_2	3	3018.5292(26)
v_4	F_2	3	1310.761458(16)
ZPE			**9493.453(19)**

The vibration-rotation Hamiltonian of methane used in this work is based on the tetrahedral formalism detailed in reference [25]. This Hamiltonian is derived by a suitable choice of successive contact transformations, which has the advantage of reducing the extent of calculations to a set of localized vibrational states called polyads. Each of these polyads is composed of a set of vibrational states which satisfy the following relation:

$$n = 2 \ (v_1 + v_3) + v_2 + v_4$$

Equation 1

where $v_{i=1;2;3;and\ 4}$ are the vibrational quantum numbers associated to the normal modes of methane. n is the polyad quantum number. The construction of the Hamiltonian is detailed in the appendix.

2.3 Recalculation of spectral line intensities and simulation of spectra

Line intensities (in arbitrary units) calculated by Equation 16 in the Appendix are at a given reference temperature (T_{ref}). For the simulation of a spectrum they must then be recalculated at a new temperature.

If N is the number of molecules per unit volume at a given temperature T, the population N_{E1} at a given energy level E_1 (with units of energy expressed in wavenumbers, cm^{-1}), is given by Equation 2:

$$N_{E1} = \frac{g_1 N}{Q(T)} e^{-\frac{c_2 E_1}{T}}$$

Equation 2

Where g_1 is the degeneracy of the energy level, Q(T) is the total internal partition sum, and c_2 is the second radiation constant (hc/k). For simplicity, we assume a Boltzmann distribution of energy, this assumption is incorporated through the exponent term raised to the power of -1/kT. This exponent term combined with the total internal partition sum and degeneracy gives the probability of finding a molecule in a certain energy state at a given temperature. The assumption of Boltzmann distribution of the vibrational states is validated by the quality of the fit that we obtain in fitting the non-equilibrium spectra. We also attempted a two vibrational temperature fit, treating the bending modes and stretching modes separately, but this did not lead to an improved fit. It is therefore assumed that relaxation between vibrational levels in the same polyad is sufficiently fast [26,27] that a Boltzmann distribution is observed, we will discuss this further in a future work. Equation 2 can be modified to accommodate the separation of both vibrational and rotational temperatures, with the new terms describing the probability of finding a molecule in a given vibrational or rotational energy state, by Equation 3:

$$N_{Evib,Erot} = N \frac{g_v}{Q_v(T_{vib})} \frac{g_r}{Q_r(T_{rot})} e^{-\frac{c_2 E_{vib}}{T_{vib}}} e^{-\frac{c_2 E_{rot}}{T_{rot}}}$$

Equation 3

Where Q_v and Q_r are the vibrational and rotational partition sums, g_v and g_r are the vibrational and rotational degeneracies. $N_{Evib,Erot}$ is the population density of the molecule in a given combination of vibrational and rotational energy level at a given vibrational and rotational temperature.

For any given temperature the Raman signal intensity (I) is linearly proportional to the population density (N) of that level, i.e. $I_T \propto kN_T$. The difference in Raman signal intensity between two different temperatures (I_1 and I_0) is the ratio of the population density at the new temperature (N_1) to the initial temperature (N_0):

$$I_1 = I_0 \frac{N_1}{N_0}$$

Equation 4

Substituting Equation 3 into Equation 4, it follows that:

$$I_1 = I_0 \frac{Q_{v,0} Q_{r,0}}{Q_{v,1} Q_{r,1}} \exp\left(-\frac{c_2 E_{rot}}{T_{rot,1}} - \frac{c_2 E_{vib}}{T_{vib,1}} + \frac{c_2 E_{rot}}{T_{rot,0}} + \frac{c_2 E_{vib}}{T_{vib,0}}\right)$$

Equation 5

Where the term containing the partition sums is constant for all spectral lines at any calculated temperature, and is therefore only important in calculating absolute line intensities. For the benefit of simplicity, it can safely be ignored provided that the Raman spectrum to be fit is normalised.

This leaves:

$$I_1 = I_0 \exp\left(-\frac{c_2 E_{rot}}{T_{rot,1}} - \frac{c_2 E_{vib}}{T_{vib,1}} + \frac{c_2 E_{rot}}{T_{rot,0}} + \frac{c_2 E_{vib}}{T_{vib,0}}\right)$$

Equation 6

Here, E_{rot} can be calculated for any rotational level, and for a spherical top molecule is given by (Herzberg, Molecular spectra II):

$$E_{rot} = BJ(J + 1)$$

Equation 7

The rotational constant, $B_{v=0}$, is 5.2412 cm^{-1} for CH_4 [28]. We assume that for any given rotational temperature, that the rotational levels are thermodynamically populated for all vibrational levels. This is reasonable since rotational redistribution occurs on timescales similar to the collision frequency [27].

E_{vib} is given by the vibrational energy for each vibrational quantum number at J = 0, this is calculated by:

$$E_{vib} = \left(E_{v_1} v_1\right) + \left(E_{v_2} v_2\right) + \left(E_{v_3} v_3\right) + \left(E_{v_4} v_4\right)$$

Equation 8

Where v_i is the vibrational quantum number for the ith vibrational mode. The energy for each vibrational mode at J = 0 is: E_{v1} − 2771 cm^{-1}, E_{v2} − 1444 cm^{-1}, E_{v3} − 2930 cm^{-1}, E_{v4} − 1282 cm^{-1}. In this calculation, we treat the molecule as a harmonic oscillator so that the energy of the vibrational level is a simple sum of the contribution of individual vibrational modes.

Equation 6 is used to recalculate all line intensities relative to the reference temperature. This gives a line spectrum that is converted to a simulated spectrum by applying a line shape function, e.g. Gaussian lineshape at the resolution of the spectrometer.

2.4 Spectral Fitting Routine

The Levenberg-Marquardt method based Python fitting algorithm LMFit [29] is used to iteratively find best fit values of T_{vib} and T_{rot} for an experimental spectrum. Note that the Levenberg-Marquardt algorithm finds a local minimum, however, testing of both equilibrium and non-equilibrium spectra shows that in our test cases the best fit is a unique solution. The fitting algorithm uses the spectral lines calculated with the STDS software at a given reference temperature as an input. The iterative part of the algorithm works as follows:

1. On each iteration, the spectral line intensities are recalculated at a test T_{vib} and T_{rot}.
2. The recalculated spectral lines are converted to a simulated spectrum. A lineshape function is applied to each individual spectral line. The sum of all of these simulated spectral lines gives the spectrum. This spectrum is calculated at discrete wavenumber values corresponding to the data points of the experimental data being fit.
3. The residual between the simulated spectrum and experimental spectrum is calculated, weighted by the scaling function given in Equation 9.
4. The iterative process repeats, testing new values for T_{vib} and T_{rot} until a local minimum value of the residual is obtained.

T_{vib} and T_{rot} are constrained to be in the range of 250 K to 3000 K, but unconstrained in relation to each other. The fitting algorithm uses a weighted fitting function to reduce the magnitude of the residuals that are caused by the uncertainty in the calibration of the spectrometer resolution. Specifically, these large residuals tend to occur at regions with steep gradients in signal intensity. Hence, the normalised derivative of the signal is used to limit the effect of these regions. This scaling function is given by:

$$Scaling\ function = \sqrt{S}\left(2 - \frac{\left|\frac{dS}{dv}\right|}{Max\left(\frac{dS}{dv}\right)} \right)$$

Equation 9

The scaling function is applied to simulated spectra in the region from 300 – 1500 K, from these spectra the mean scaling function is determined, and smoothed using a 2nd order Savitsky-Golay filter with a ~0.75 cm^{-1} window.

If a weighting of this region is not used, the error in fitting T_{rot} blows up due to the large residual from fitting the Q-branch of the ground state v_1 transition at 2917 cm^{-1}. To fit this without weighting is dependent on having a very accurate measurement of the lineshape function parameters, which was not possible when fitting the data of Magnotti [30].

2.5 Calculation of error

The confidence intervals are determined by calculating the 3σ (99.7% probability) of temperature using the F-test, an iterative process of error determination that applies the Levenburg-Marquardt fitting procedure described previously. In the F-test the null hypothesis (i.e. the best fit) is compared with alternative model solutions by changing parameter values and observing the change in chi-squared, giving an F-value. This F-value can be used to calculate a probability distribution, and thus give the confidence intervals for the fit. The F-test is useful in calculating confidence intervals for non-Gaussian error distributions [31].

The F-test formula [29] is given in Equation 10 :

$$F\left(P_{fix}, N - P \right) = \left(\frac{\chi_f^2}{\chi_0^2} \right) \frac{N - P}{P_{fix}}$$

Equation 10

Where χ_0^2 is the chi-squared value for the calculated best fit, χ_f^2 is the chi-squared for a fit model that is being tested, N is the number of data points, P is the number of parameters, and P_{fix} is the number of fixed parameters.

By this method, the relative error on the fit of the sample spectra for both T_{vib} and T_{rot} is up to 10%. It is important to stress that in this case the confidence intervals are determined for the fit, not for all of the contributing errors

in the measured or simulated spectrum. I.e. the fitted spectrum does indeed give the best fit of the spectral data, but the calculated errors are purely statistical and do not consider contributions from systematic error.

3.0. Experimental Method
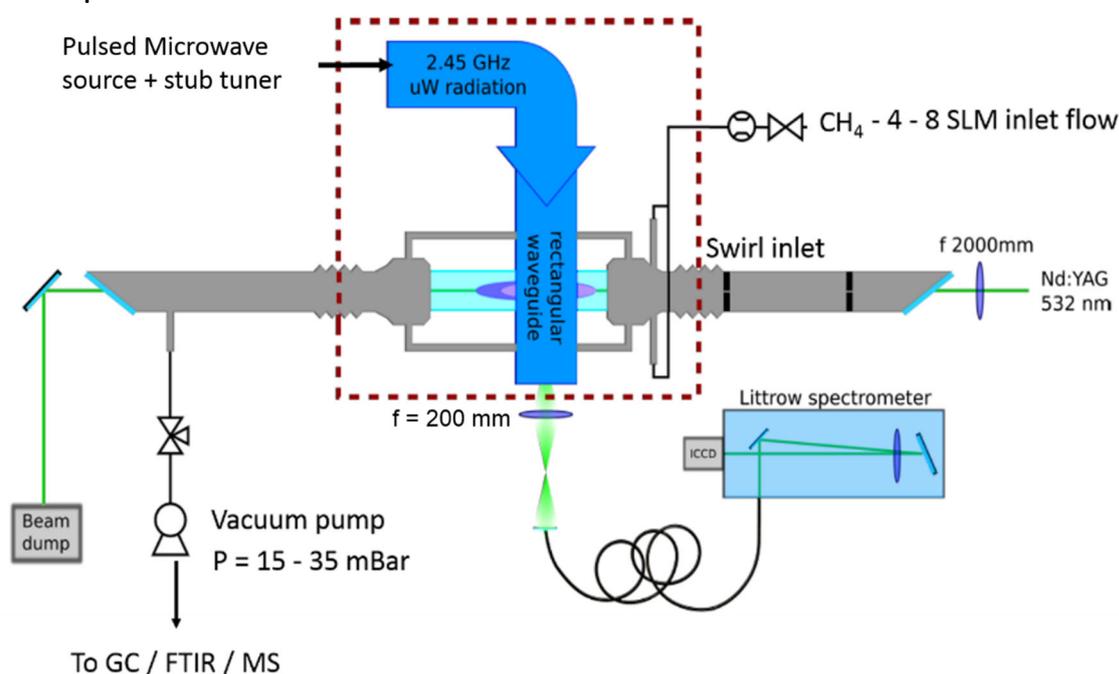
Figure 1: The Microwave plasma with laser scattering set-up

Specific details of the laser scattering and microwave discharge system can be found elsewhere [10]. In brief, a 2.45 GHz solid state microwave source is used to generate the plasma. The microwaves propagate through WR340 waveguides so that a standing wave is generated in the centre of a 26 mm ID quartz tube where the plasma is generated. The maximum plasma length is constrained by the waveguide, giving a plasma length up to 34 mm and a maximum diameter of 26 mm. The microwave source is pulsed at a repetition frequency of 30 Hz, with a pulse duration of 200 µs or less, therefore inter-pulse time is 33.1 ms. Undiluted methane at a fixed flowrate of 4 SLM and a pressure of 25 mBar flows into the quartz tube reactor via tangential gas injection. At this gas pressure and flowrate, the residence time of gas in the reactor (assuming plug flow and no gas heating) is on the order of 1 to 5 ms. The inter-pulse time greatly exceeds the gas residence time in the reactor, and therefore every time a pulse of MW power is applied the plasma reignites from gas at ~300 K, with the majority of electrons, ions and excited species depleted between pulses. This is confirmed by time resolved imaging of the plasma.

The Raman signal is generated using a frequency doubled Nd:YAG laser (532 nm), pulsed at a repetition frequency of 10 Hz, with a pulse duration of approximately 8 ns at an energy up to 600 mJ per pulse. The beam is focussed into the approximate radial centre of the plasma using an f = 2 m focal length lens such that the beam is in focus over the entire length of the plasma and into the downstream gas. The scattered light is collected using a linear array of 27 x 400 µm fibres, positioned perpendicular to the beam and focussed using a f = 200 mm lens. In order to filter out the Rayleigh component and to protect the ICCD camera from intense laser light, a 534nm long pass filter is positioned between the beam and the collection optics. The light from the fibres is passed into Littrow spectrometer, built in house, that is optimised to give maximum signal intensity.

A resolution around 0.6 cm^{-1} is required in order to resolve the different vibrational modes in the hot bands. In order to achieve this the light passes into the spectrometer through a 50 µm slit and is projected onto a 12 x 12 cm, 1800 grooves /mm grating through a 200 mm diameter, f = 1.0 m achromatic doublet. The dispersed light is refocussed onto a PI-Max4 emICCD with an electronically cooled 512 x 512 pixel array. The lineshape function is determined using a spectral line at ~630 nm from a Neon calibration lamp, which is close to the Stokes-Raman shifted CH_4 Pentad region for a 532 nm laser. At 300 K and 25 mBar, using 6 W of laser power and full emICCD

gain, the CH_4 pentad region saturates the camera within 2400 acquisitions, or 4 minutes at 10 Hz laser pulse repetition frequency.

A function generator sends the repetitive pulse waveform to the solid state MW amplifier. This function generator also acts as a master clock to a delay generator (SRS-DG645) that is used to trigger the laser flash lamps, Q-switch, and ICCD camera. Controlling the delay between the function generator trigger signal and the triggering of the laser and camera allows the generation of time resolved Raman spectra of the pulsed plasma discharge.

4. Results

4.1 Obtaining T_{vib} and T_{rot} from the Pentad

Figure 2 shows the equilibrium temperature dependence, from 300 – 1500 K, of the CH_4 pentad region without a polariser (from 2800 cm^{-1} to 3050 cm^{-1}). Within the Pentad region, the dominant peaks that are visible are Raman transitions of the symmetric stretch mode (v =1) at around 2916 cm^{-1} Raman shift, and the asymmetric stretch mode (v=3) at around 3020 cm^{-1}. The intensity of Raman transitions in the symmetric stretch mode exceeds that of the asymmetric stretch by approximately 10 times (Figure 3), giving a significant advantage in signal intensity, particularly at high temperatures or low gas pressures where the signal can be very weak due the low gas density.

As gas temperature is increased from 300 to 1500 K, new peaks appear at lower wavenumbers. For the symmetric stretch mode these are the so-called "hot bands" that are of particular interest for temperature measurement, and are used in this article to determine both rotational and vibrational temperatures independently.
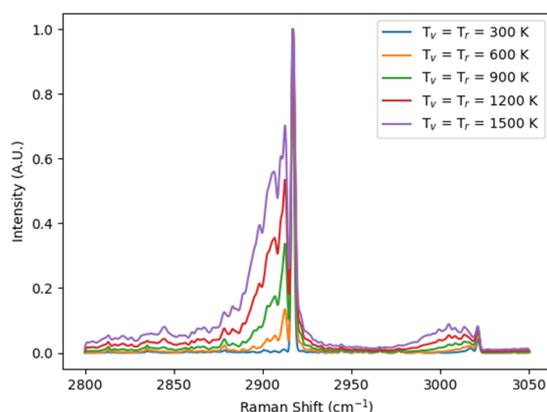
Figure 2. Simulated thermal equilibrium spectra in the CH_4 pentad region without a polariser. Resolution is set to 0.5 cm^{-1} with a Gaussian lineshape function.

The pentad region is particularly complex, featuring around 3.5 million spectral lines in this simulation. It is therefore insightful to break down the Raman spectrum into its vibrational constituent components, in order to understand the information that is contained within a spectrum.
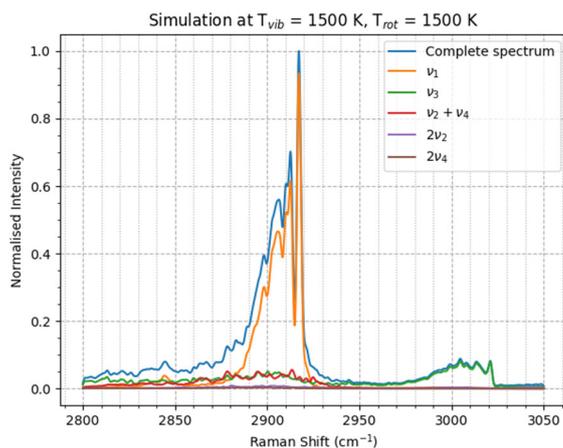
Figure 3: The Pentad region is dominated by the symmetric stretch mode (v_1) transition with the peak centre at 2917 cm^{-1}, followed by asymmetric stretch (v_3) transition centred at 3020 cm^{-1}. Spectrum simulated with 0.5 cm^{-1} resolution at T = 1500 K, without a polariser.

Figure 3 shows a simulated spectrum at 1500 K, with the different Raman transitions that contribute to the overall spectrum isolated. For the spectral region around 2850 – 2950 cm^{-1}, the main contributing component are v_1 transitions (~ up to 90% of the spectral intensity, relative to the strongest peak), followed in approximately equal proportion by v_3 and $v_2 + v_4$ (~5% each), with the overtones bending modes, $2v_2$ and $2v_4$, making an insignificant contribution to the overall spectrum.

The peak at 2970 – 3020 cm^{-1} is almost entirely composed of Raman transitions of the asymmetric stretch mode, v_3. However, this signal intensity in this spectral region is approximately 1/10th of the signal of v_1 region (2830 – 2930 cm^{-1}), which makes it less interesting for temperature measurement applications where signal intensity is important.
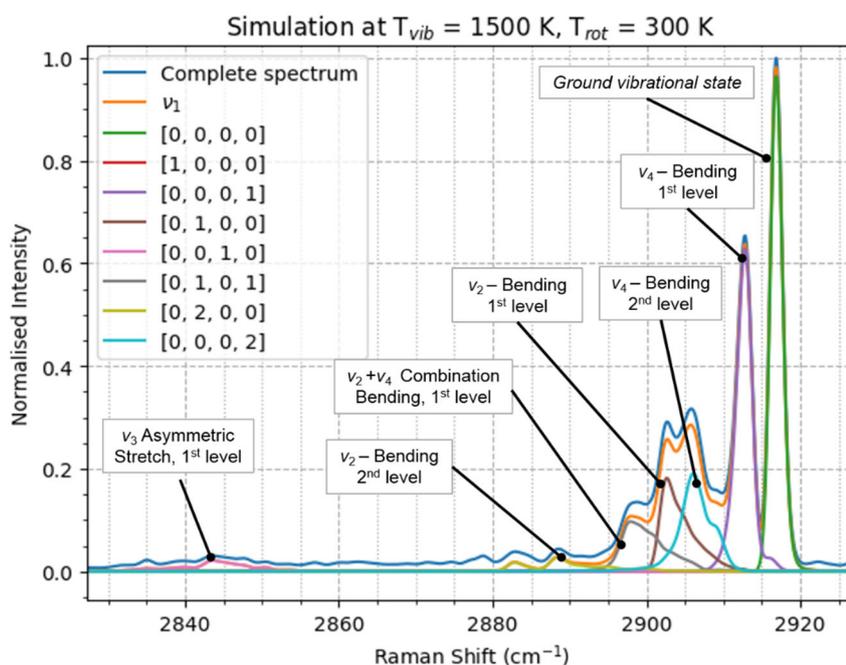
Figure 4: The v_1 cluster of peaks (including. the "hot bands") can be further broken down by the lower state vibrational level. Shown here is the complete Raman spectrum (blue), the total contribution of v_1 transitions (orange), and a breakdown of lower state energies that contribute to v_1. Green represents the ground state vibrational level. All of the peaks from 2880 – 2915 cm^{-1} originate from excitation of the bending modes, v_2 and v_4. Transitions in v_1 from the 1st level of the asymmetric

stretch mode sits at around 2830 – 2840 cm^{-1}. Note, this spectra is simulated at high T_{vib}, low T_{rot} to allow good separation of spectral peaks

A further break down of the vibrational modes that contribute to the v_1 Raman transition and complete spectrum are shown in Figure 4. We follow this line of enquiry, as being able to quantify vibrational excitation of the stretching or bending modes of CH$_4$ may be of particular interest to the plasma chemistry and catalysis communities [32–36].

The numbers indicated in square brackets show the lower vibrational state of CH$_4$. The spectrum is simulated at a high T_{vib} and a low T_{rot} in order to make the spectrum less complex and therefore easier to read. A summary of the Raman transitions observed highlighted in Figure 4 is given in Table 2.

Table 2: Low temperature Raman transitions observed in the Pentad region (around 3000 cm^{-1}), corresponding to ±2 change in the Polyad number.

Polyad Transition	Upper State [v_1, v_2, v_3, v_4]	Lower state [v_1, v_2, v_3, v_4]	Approx. Band Centre (cm^{-1})
P2 – P0	1,0,0,0	0,0,0,0	2916
P3 – P1	1,1,0,0	0,1,0,0	2902
	1,0,0,1	0,0,0,1	2912
P4 – P2	1,1,0,1	0,1,0,1	2888
	1,2,0,0	0,2,0,0	2884
	1,0,0,2	0,0,0,2	2906
	1,0,1,0	0,0,1,0	2842
	2,0,0,0	1,0,0,0	N/A

The fundamental peak at 2916 cm^{-1} is predominantly formed from methane in the ground vibrational state, corresponding to the Raman transition (1000) → (0000) , or P2 – P0. At vibrational temperatures of 1500 K, the hot bands of the spectrum are primarily caused by excitation of the methane bending modes (v_2 and v_4). For excited v_4, the (1001) → (0001) transition at 2912 cm^{-1} and (1002) → (0002) at 2906 cm^{-1} make some of the largest contributions to the overall spectrum. This is closely followed by contributions from the (1100) → (0100) transition at 2902 cm^{-1}, and the combination bending mode, $v_2 + v_4$, (1101) → (0101). Remarkably, stretching modes do not make a significant contribution to the Raman spectrum at this vibrational temperature. The 1st vibrational level of the symmetric stretch mode, (2000) → (1000) or P4 – P2, has transitions appearing at 2884 cm^{-1}, 2997 cm^{-1} and 3023 - 3032 cm^{-1}, with a relative maximum peak height of 0.00027.

The v_1 Raman transition for the 1st vibrational level of asymmetric stretch mode, (1010) → (0010), peak appears centred at 2842 cm^{-1}. This peak is sufficiently well resolved that it may be possible to obtain a stretching mode vibrational temperature in addition to a bending mode vibrational temperature. In this article, we do not attempt to separate the stretch vibrational temperature from the bending vibrational modes. This is because, 1 - it occurs outside of the spectral range of a single shot acquisition with our spectrometer, and 2 – if the vibrational levels are thermodynamically distributed, the stretch vibrational temperature would have to be very high (~1500 K) for the signal intensity to significantly exceed that of the P and O branch of the v_3 transition, and 3 – the treatment of combined stretching and bending vibrational modes is difficult. The remainder of this work focusses on the hot bands, formed in the 2880 – 2910 cm^{-1} region, that are primarily caused by bending vibrational modes being populated.

Following the study of which vibrational modes contribute to the hot band, we now examine how non-equilibrium between vibrational and rotational excitation appears by changing vibrational and rotational temperature independently.
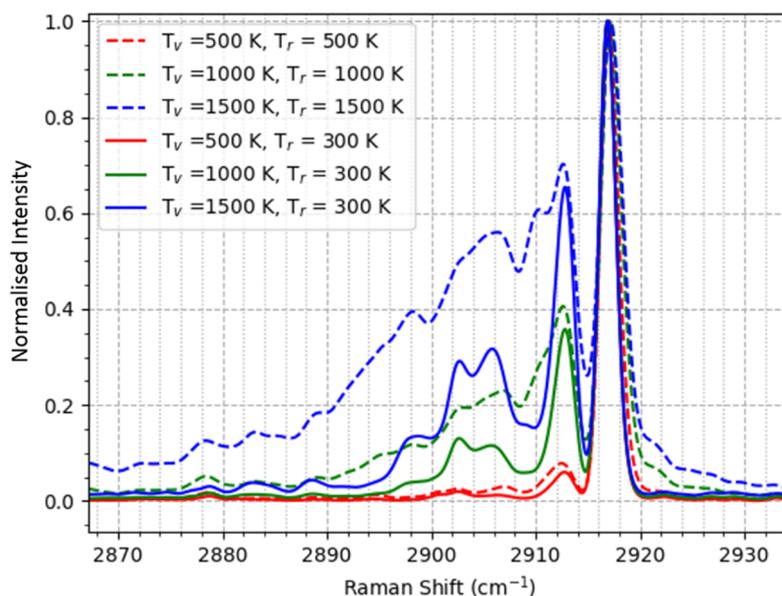
Figure 5: Non-equilibrium (solid lines) and equilibrium (dashed lines) simulated with changing T_{vib}. Increasing T_{vib} leads to more vibrational modes being populated, therefore as T_{vib} increases new peaks appear. As T_{rot} increases, rotational levels within the vibrational mode increase, hence the peaks of the vibrational levels become broader. Spectra are normalised so maximum intensity of each spectrum = 1.

Figure 5 show the influence of increasing temperature at thermal equilibrium (dashed lines), compared with spectra in which vibrational temperature exceeds rotational temperature (solid lines). From examining the solid lines of the same colour have equal vibrational temperatures. For example, comparing the blue lines, where T_{vib} = 1500 K, and T_{rot} = 1500 K (dashed line) or 300 K (solid line), it is clear that the increase in rotational temperature causes a significant change in the shape of the band, with a considerable broadening due to higher rotational levels being populated. Similarly this can also be observed with the green lines (T_{vib} = 1000 K) and the red lines (T_{vib} = 500 K), albeit to a lesser extent with decreasing ratios of non-equilibrium between T_{vib} and T_{rot}. At the lowest non-equilibrium simulated here, shown in red, (where T_{vib} = 500, T_{rot} = 300) the difference in the shape of the band appears small compared with the equilibrium case (T_{vib} = T_{rot} = 500 K).

This raises the question of sensitivity when fitting data when only a weak non-equilibrium is present. Typically, in spontaneous Raman scattering at low pressures and high temperatures there is a balance between having either sufficient resolution or sensitivity. In this case it is critical to have a sufficient resolution to be able to observe changes in peak shape, without losing sensitivity due to a poor S/N ratio. Raman transitions of v_1 are relatively strong, with a relative cross section ~5.6 times higher than N_2 [37]. This allows some flexibility in obtaining the required resolution to resolve the vibrational bands and thus have the sensitivity to fit the spectrum.
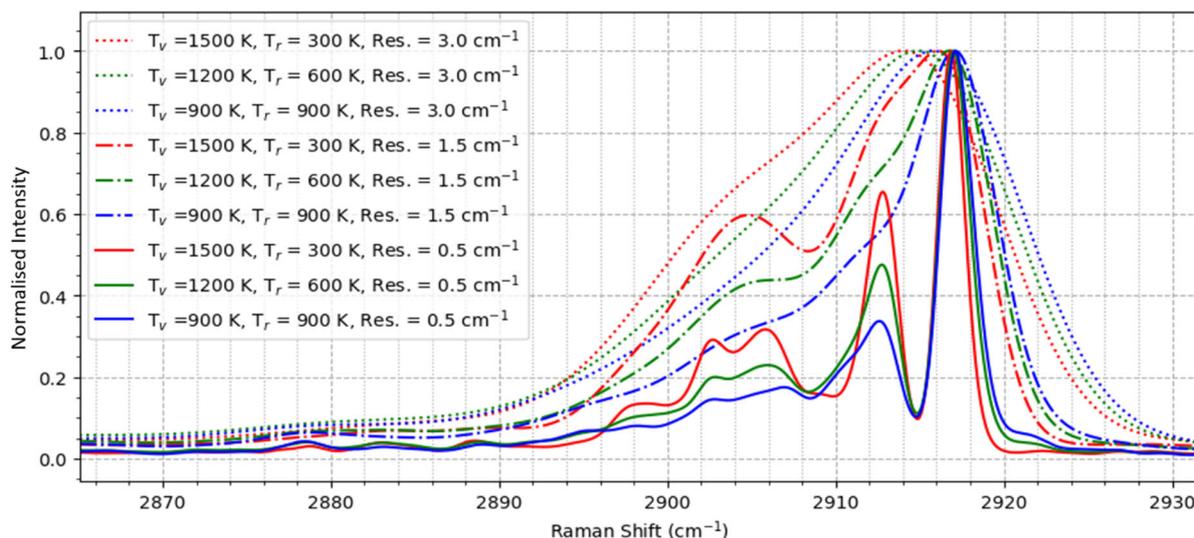
Figure 6: The effect of spectrometer resolution on the convolution of peaks around the v_1 transition. Only when the resolution is approximately 0.5 cm^{-1} is it possible to fully resolve the structure of the hot bands, which is required to reliably fit T_{vib} and T_{rot}. Spectra are normalised, so maximum intensity for each spectrum = 1. The resolutions selected reflect the capabilities of our spectrometer, where 3.0 cm^{-1} would be the spectrometer with no slit, and ~0.5 cm^{-1} is the expected resolution with a ~50 μm slit.

Figure 6 shows simulated spectra for a range of realistic spectrometer resolutions, 3 cm^{-1}, 1.5 cm^{-1}, and 0.5 cm^{-1} with a Gaussian lineshape function. Three different temperature combinations are depicted: a strong non-equilibrium (red line, T_v = 1500 K, T_r = 300 K), a moderate non-equilibrium (green line, T_v = 1200 K, T_r = 600 K), and a thermal equilibrium (blue line, T_v = 900, T_r = 900 K). These temperature combinations are deliberately chosen to be extreme in order to emphasise the importance of resolution in fitting these spectra.

At 0.5 cm^{-1} (FWHM = 1 cm^{-1}) resolution (solid line) the shape of the hot band is well resolved, and distinct peaks at 2913 cm^{-1} and 2917 cm^{-1} are observed. This is significant as the peak at 2917 cm^{-1} is the (1000) → (0000) transition, and the peak at 2913 cm^{-1} is the (1001) → (0001) transition. The 1st vibrational level of the v_4 bending mode, i.e. (0001), being the lowest available vibrational energy level above the ground state, hence it is populated first during gas heating. Furthermore, there is an acceptable separation between the cluster of peaks around 2896 – 2908 cm^{-1} and the peak at 2913 cm^{-1}.

As the resolution is decreased, to 1.5 cm^{-1} (dot-dash line), the separation of distinct spectral peaks is no longer possible. The previously observed peaks at 2913 and 2917 cm^{-1} are convoluted, but some separation of the 2896 – 2908 and the 2913 cm^{-1} peaks remains. It is likely possible to fit spectra at this resolution, but much of the structure of the spectrum is lost.

At a resolution of 3 cm^{-1} (dotted line), all of the peaks are entirely convoluted, and no structure remains to the hot bands. Errors on vibrational and rotational temperature fitting in this condition are likely to be large. To summarise, a resolution of approximately 0.5 cm^{-1} is sufficient to resolve the vibrational structure of the pentad hot bands, and thus obtain a measurement of T_{vib} and T_{rot}.
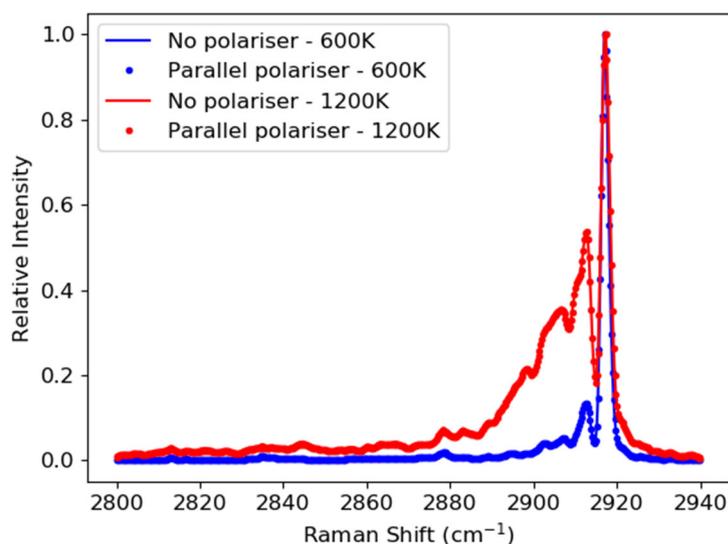
Figure 7: Spectral simulation at two temperatures shows that the presence of a polariser that is oriented parallel to the incident radiation has a minimal effect on the spectrum in the hot band region of the Pentad.

Finally, the use of a polarisation filter in the collection of the Raman spectra is considered. 7 shows a comparison between the normalised Raman spectra simulated with and without a parallel polariser, plotted at 600 and 1200 K. In this spectral region and at this scale of intensity, the difference between the two polarisation cases is virtually indistinguishable. This is because the v_1 transition, which is the predominant spectral feature in the region, has a depolarisation ratio of 0. However, the use of a polarising filter can result in a significant loss of signal due to signal attenuation of the transmitted polarisation by the filter (transmissivity of available polariser at 600 nm = 70%), in addition to filtering 4/7 of the anisotropic component of the spectrum [38]. We therefore opted not to use a polarising filter in the collection of the spectra in our experiments, since it increases acquisition time and decreases signal to noise ratio at high temperatures. It should also be noted that the difference in fitting of the spectrum with and without parallel polariser is negligible.

4.2 Validation of method by fitting equilibrium spectra
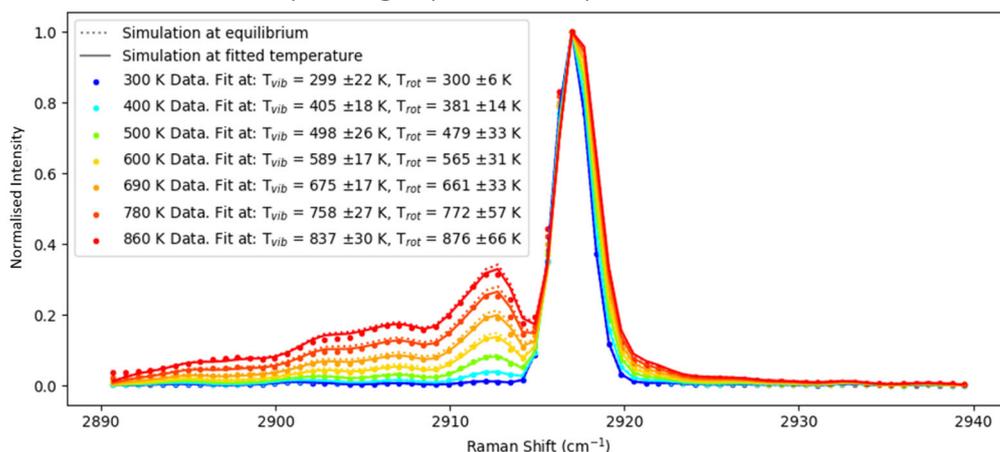
Figure 8: Spectra simulated at thermal equilibrium (dotted line) and the calculated temperature fit (solid line), compared with the Magnotti data (data points). Note that the Magnotti data is acquired using a parallel polariser, hence the data is fit using the parallel polarised line lists.

In order to validate the fitting procedure, the fitting routine is applied to thermal equilibrium spectral data at temperatures in the range of 300 – 860 K from Magnotti et al. [30] (hereafter referred to as the equilibrium spectra). The known temperature (T_{exp}) data from the equilibrium spectra (dots), a simulation at the experimental temperature and at calculated temperatures are shown in Figure 8. By fitting the 300 K equilibrium spectrum, their spectrometer resolution is found to be 0.6 (± 0.05) cm^{-1} with a Gaussian lineshape, this is subsequently

convoluted with a pixelated lineshape due to the limited resolution of the ICCD. Assuming the equilibrium spectra Raman shift is calibrated on the peak position of the v_1 transition at around 2917 cm^{-1}, the pixelation of the spectrum can also lead to a small offset in apparent peak centre from the actual peak centre. In the fitting of the spectra this is constrained to be ±1 cm^{-1}.
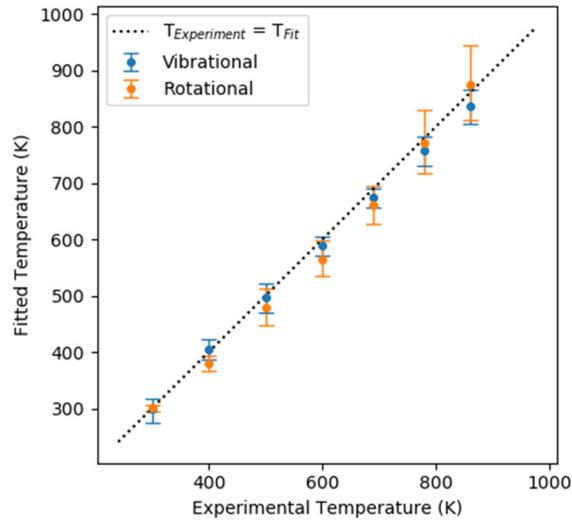
Figure 9: Comparison of the fitted values of T_{vib} and T_{rot} with the measured experimental temperature from the data of Magnotti et al. Ideally, all of the pairs of data points in the plot should sit on the dashed line (T_{exp} = T_{fit}) or top of each other, indicating the expected thermal equilibrium. The error bars show that the 3σ (99.7%) confidence interval, determined by applying the F-Test within the LMFit algorithm. The error shown in this plot is the calculated error of the fit, and does not include the error due to the calculation of the lineshape function, the calculation of the stick spectrum, or experimental error in the data of Magnotti.

Across the entire temperature range of available spectra the fitted spectra of the thermal equilibrium data returns the correct temperature value (Figure 9). At every temperature the fit returns values for T_{rot} and T_{vib} that fall within, at most, 40 K of each other, and within the calculated 3σ confidence interval for the fit. At some temperatures the experimental temperatures falls just outside the confidence interval of the calculated temperature. This is indicative of other contributing errors, possibly in the data of Magnotti, the calculation of the stick spectrum, or calibration of the lineshape function. In order to compensate for these additional sources of error, we take a cautious approach of stating that the maximum relative error in the calculated confidence intervals is the error that should be applied in all instances that the fitting algorithm is applied. The relative deviation of the calculated fit and confidence intervals from the reported equilibrium temperature are plotted in Figure 9. The maximum relative deviation of ±10% (see Figure 9) from the reported actual experimental temperature occurs at 600 K. In applying this algorithm to fit non-equilibrium spectra, the relative error is therefore assumed to be equal to this maximum value of 10%. This error is dependent on the resolution of the system, consequently this 10% error is only valid when the spectral resolution is 0.6 cm-1 or lower.
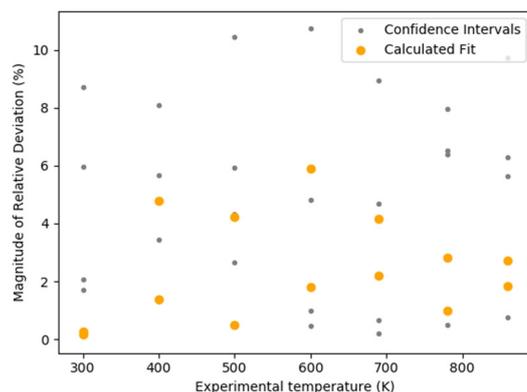
Figure 10: The relative deviation of the confidence interval and the calculated fit from the experimental temperature. The maximum relative deviation is ±10%, which, in addition to the fitting error, should be applied when estimating error on calculated temperatures.

As temperature increases up to 860 K, the difference between T_{vib} and T_{rot} increases up to 20 K (T_{exp} = 860 K, T_{vib} = 842 ± 14 K, T_{rot} = 861 ± 35K). With increasing temperature the magnitude of the confidence intervals also increases, although this has an insignificant influence on the relative deviation of the calculated temperature (Figure 10). As such, we recommend using a flat 10% relative error on calculated temperature in addition to calculating the fitting error. This gives a cautious estimate of the error, which is appropriate given the inherent non-linearity of the simulated spectra.
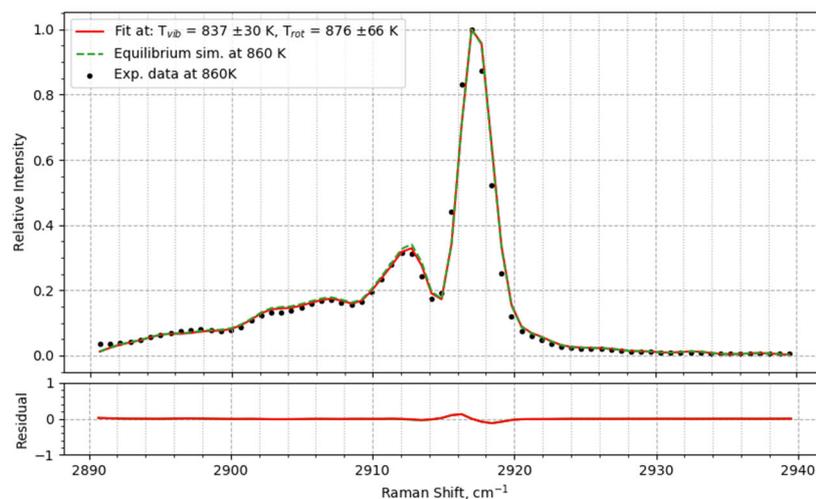
Figure 11: Simulation at the calculated temperatures and at 860 K compared with the data recorded by Magnotti. The difference between the two simulated spectra is very small, with the fit result returning a marginally smaller residual in the 2900 – 2915 cm^{-1} region. Note the large residual around the central peak (2917 cm^{-1}), this is due to error in fitting the lineshape of the 300 K spectrum.

It is worth noting that the small difference in temperature between the calculated and equilibrium spectrum translates to a small difference in the resultant spectrum. This point is illustrated by the spectra in Figure 11, which shows the experimental data (black points), the fit (red line) and the simulation at 860 K (green line), and their respective residuals. The difference in residual between the fitted spectrum and the spectrum simulated at 860 K occurs predominantly in the range 2900 – 2915 cm^{-1}, and is relatively small, having a maximum difference between each other of approximately 1% of the total spectrum.

The accuracy of the fitting routine in independently finding both vibrational and rotational temperatures for the data of Magnotti demonstrates the validity of this method at temperatures up to 860 K. The authors state that above 860 K, there are regions in the gas flow where the local temperature is in excess of the measurement temperature, which can result in thermal decomposition of CH4 and the creation of other hydrocarbon species. Raman activity in the 3000 cm-1 spectral region is a common feature of many hydrocarbons, as is discussed in

the next paragraph. Whilst it is not possible to validate this method up to higher temperatures against known temperature spectral data, we believe that it is valid at least up to 1500 K due to the validation of similarly calculated (but not fitted) Raman spectra reported in [38] using coherent anti-stokes Raman spectroscopy (CARS).

The possibility of interference from other hydrocarbon molecules [30,39] and radicals [40,41] in the spectral region of interest is an important consideration, and impacts the applicability of this method to systems where other species do not heavily influence the observed spectrum. Intense peaks around 3000 cm^{-1} caused by the C-H stretch vibration are common amongst the Raman spectra of many hydrocarbons, some possible species with known Raman spectra are listed in Table 3. Of the various species listed ethane (C_2H_6) and propane (C_3H_8) are of the most concern as they have strong Raman active peaks in the centre of the CH_4 hot bands. For example, 0.57% C_2H_6 balanced with CH_4 would have intensity of 1% of the strong CH_4 peak at 2917 cm^{-1}. This *could* influence the shape of the spectrum, and therefore influence the calculated fit and measured temperature for T_{vib} and T_{rot}. In order to evaluate this possibility, the fitting procedure is applied to the equilibrium data (at 400 K) contaminated with different mole fractions of C_2H_6 up to 10% in CH_4 (Shown in supplementary information S1). With all of the tested data sets the calculated value of T_{vib} and T_{rot} fall within 10% of each other and the actual experimental temperature. Therefore the presence of a small concentration of C_2H_6 (up to 10%) on the spectral shape of the methane hot bands is insignificant, and does not have a significant effect on the calcualated temperatures.

In the pulsed plasma experiments described, it is therefore extremely unlikely that product species or intermediates lead to the characteristic "vibrational excitation" peak that occurs at 2913 cm^{-1} for a number of reasons:

1 - A significant concentration of ethane or propane is not able to form during the early phases of the pulse (<70 μs), simply due to having insufficient time for reaction

2 - Following GC-FID and FTIR analysis no ethane or propane is detected

3 – Fitting the spectra corresponding to C_2H_6 concentrations up to 10% would not give the vibrational-rotational non-equilibrium observed in our experiments.

*Table 3: Hydrocarbon species with known vibrational frequencies and Raman activity in the 3000 cm^{-1} region. This list is not limited to the species identified here. *Cross section is given relative to methane. Please treat with caution the relative cross section values adapted from [39], which has large errors in reported Raman shift for each species. ⁺Methyl Raman shift reported values from literature range from 2992.6 – 3002.4. C_2H_2 is not included in the table as it has no Raman transitions in the 3000 cm^{-1} region.*

Species	Transition	Raman shift (cm^{-1})	Relative cross section*	Concentration to give 1% signal magnitude relative to CH_4 (%)	Ref.
Methane, CH_4	ν_1	2917	1.0	N/A	[39]
Ethane, C_2H_6	ν_1	2954	1.7	0.57	[30,39,42]
	$2\nu_8$	2899	1.0	1.00	[30]
Propane, C_3H_8	Various	2887-2971	2.2	0.43	[39]
Ethylene, C_2H_4	ν_1	3020	0.7	1.33	[39]
Methyl, CH_3	ν_1	3002±1⁺	-	-	[40]

4.3 Fitting vibrational-rotational non-equilibrium spectra

Having demonstrated that it is possible to fit equilibrium spectra to obtain accurate values for T_{vib} and T_{rot}, we extend the application to fitting non-equilibrium spectra. As it is not possible to produce non-equilbrium spectra with known temperature values, the aim of this section is to demonstrate that non-equilibrium temperature values do indeed give the best fit result. In order to demonstrate this, CH_4 spectra generated in the low duty cycle pulsed microwave plasma are used.
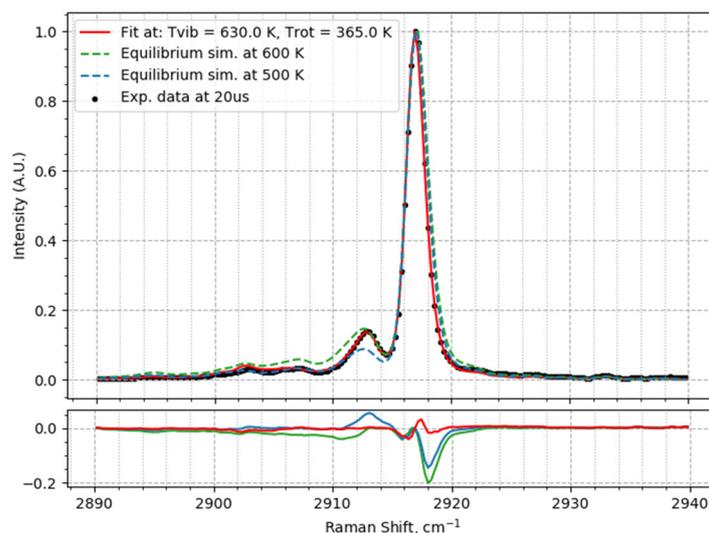
Figure 12: Plasma generated spectrum (black dots) at 20 us into a pulse, fitted (red line) with T_{vib} = 630 (± 63) K, T_{rot} = 365 (± 36) K. Imposing an equilibrium fit tends to over or underestimate the peak height over a wide spectral range, whereas fitting a non-equilibrium spectrum reliably gives a good fit for the experimental data. Spectrum recorded without a polariser, using maximum emICCD gain with 1800 on CCD accumulations, corresponding to a 3 minute acquisition time at 10 Hz laser pulse frequency.
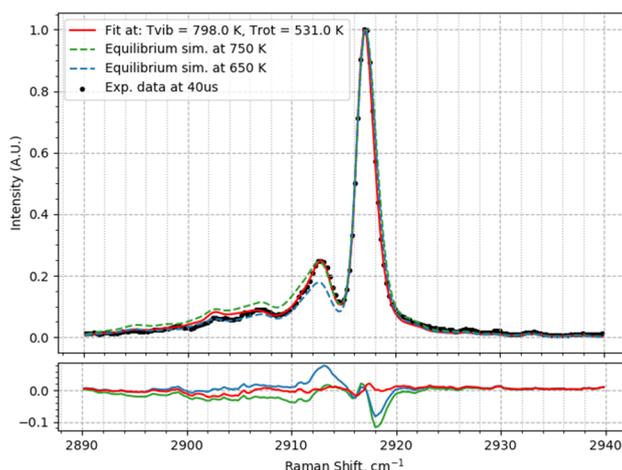
Figure 13: Non-equilibrium spectra obtained at 40 μs into a plasma pulse fitted with T_{vib} = 798 (± 80) K, T_{rot} = 531 (± 53) K. Comparing equilibrium temperature simulations, and non-equilibrium simulations the fit residuals are similar to the plot shown in Figure 12. Spectrum recorded without a polariser, using maximum emICCD gain with 1800 on CCD accumulations, corresponding to a 3 minute acquisition time at 10 Hz laser pulse frequency.

The vibrational and rotational temperatures in the plasma increase with the power input and duration of the plasma. t = 0 μs is defined as the point at which microwave power is first applied to the reactor. Ignition happens at approximately 10 μs into the pulse, following which electron collisions with CH_4 lead to the generation of vibrationally excited CH_4 molecules [12,43]. Within 70 μs, gas heating leads to a vibrational-rotational equilibrium being re-established. Within the 60 μs between ignition and equilbrium, it is possible to record non-equilibrium CH_4 spectra. The specific heating mechanisms that lead to the equilibration of vibrational and rotational temperature are complex, having a number of possible mechanisms and will there be addressed in a future work. beyond the scope of this work.

Two different non-equilibrium spectra are presented, one at 20 μs into the pulse (Figure 12) and another at 40 μs (Figure 13). With each spectrum the experimental data (black dots) and the simulated fitted spectrum (red) are shown, as well as two simulations at equilibrium (blue, green, purple), and the residuals of the various simulations. The calculated lineshape function of the spectrometer at this wavelength is a Voigt profile, with σequal to 0.49 cm^{-1} and γequal to 0.29 cm^{-1}. Where σ is the Gaussian compoenent of the line broadening, and γ

is the Lorentzian component; please refer to the appendix for further information on the calculatiomn of the Voigt profile.

A qualitative way to asses the vibrational and rotational temperatures in the non-equilbrium spectra is by the fact that increasing vibrational temperature tends to increase the peak height of the hot bands relative to the main peak, whilst increasing rotational temperature tends to increase the apparent broadening of the peaks.

Consider the equilibrium simulations in each presented set of spectra. Taking Figure 12 first, the dashed green line shows an equilibrium simulation at 600 K. This temperature is selected so that the relative height of the hot band peak at 2913 cm^{-1} is the same as the experimental data. Looking to the left of the peak, at shorter Raman shifts (from 2900 – 2913 cm^{-1}), the simulation significantly overestimates the height of the hot-band. Similarly, the width of the central peak at 2917 cm^{-1} is overestimated, this is reflected most clearly in the very large residual at 2918 cm^{-1}. This overestimation of the peak width, both around the central peak and in the hot bands, either implies that the line shape is incorrect or that the rotational temperature in the simulation is higher than the experiment.

The dashed blue line, where $T_{vib} = T_{rot} = $ 500K, in the region from 2900 to 2910 cm^{-1} gives a good fit for the experimental data, with a residual close to zero. However, the relative height of the peak at 2913 cm^{-1} is underestimated, which from qualitative assesment implies that the vibrational temperature is too low. Additionally, the residuals indicate that the width of the central peak (2917 cm^{-1}) is still overestimated, suggesting that the rotational temperture is still too high.

This same analysis can be repeated with Figure 13, and indeed, identical trends are observed. In the higher temperature equilibrium simulations, the vibrational temperature appears to be correct, but rotational temperature is too high. Whilst in the lower temperature simuations, the rotational temperature appears to give an improved fit (but still too high), whilst the vibrational tempeprature is significantly underestimated. This exercise clearly demonstrates that an equilibrium fit cannot return a satisfactory fit for the experimental data.

Conversely, in both spectra presented the non-equilibrium fit returns an excellent fit result, where the simulated spectrum maps onto the majority of the experimental data points with only a small residual (max residual – 0.024, Figure 13). The greatest deviations in the fit from the data occur around the central peak (2917 cm^{-1}), and in the region from 2900 – 2904 cm^{-1}. For the central peak, the fitting error is most likely due to inaccuracies in the lineshape function, and regardless, the magnitude of the resiudal in the non-equilibrium case is ¼ of magnitude of the equilbirum case.

Explaining the overestimation of the peak height by the simulation around 2900 - 2904 cm^{-1} is more challenging, having a number of possible causes that include contributions from systematic error and noise, the appearance of other hydrocarbons, or alternately it may be related to some of the assumptions made in calculatiomn of the spectra. However, in our case the relative difference between the fit and the data is relatively small around this region, hence the potential error sources can be ignored without impacting the validity the assesment of non-equilibrium. However, for applications that do use this approach to obtain temperatures, particularly with a desire to obtain fit the vibrational and rotational contributions, it is imporant to be aware of the possibility of other hydrocarbons with a C-H stretch vibration in this wavenumber range.

5. Conclusions

A method to quantify vibrational and rotational temperatures from the methane spontaneous Raman spectrum in the pentad region is presented.

The positions and intensities of the spectral lines are calculated at a reference temperature (~1500 K) using the latest updated effective Hamiltonian developed in Dijon up to the Tetradecad (6200 cm^{-1}) and rotationally up to J=30. The intensities of these spectral lines are then recalculated at different vibrational or rotational temperatures, assuming a Boltzmann population distribution function. The Python based iterative fitting procedure, LMFit, is used to fit simulated spectra to experimental or sample data, returning values for vibrational and rotational temperature. In the fitting process, the two temperatures are not constrained with respect to each other, but some weighting is applied in the "hot-band" region (2900 – 2915 cm^{-1}).

This fitting and simulation of spectra is validated against published known temperature spectra from Magnotti et al [30], and returns an excellent fit with measured vibrational and rotational temperatures consistenly within a 10% relative error. Furthermore, this fitting routine is applied to CH$_4$ spectra obtained in a low pressure pulsed

microwave plasma, where a vibrational-rotational non-equilibrium can be sustained on the order of 50 µs. Using spectra recorded from timesteps within the pulsed plasma we are able to fit the methane spectrum and therefore observe and quantify the non-equilibrium between T_{vib} and T_{rot} in the plasma.

6. Appendix

The vibration-rotation Hamiltonian used in this work is based on the tetrahedral formalism detailed in [25]. Thanks to implicit contact transformations [44], the contribution of interpolyad interactions are removed to higher orders, while the intrapolyad coupling terms are explicitly taken into account. As a result, the polyads can be studied independently from each other.

The polyads, P_n, are numbered with increasing energy starting with P_0 for the Ground State (GS) or Monad, P_1 for the Dyad, P_2 for the Pentad, etc.

The resulting effective Hamiltonian of a given polyad can be written in tensorial form as a linear combination of the vibration-rotation operators such as:

$$\widetilde{\mathcal{H}}_{\{P_k\}} = \sum_{all\ indices} \tilde{t}_{\{s\}\{s'\}}^{\Omega(K,n\Gamma)\Gamma_v\Gamma_{v'}} T_{\{s\}\{s'\}}^{\Omega(K,n\Gamma)\Gamma_v\Gamma_{v'}}$$

Equation 11

The term $\tilde{t}_{\{s\}\{s'\}}^{\Omega(K,n\Gamma)\Gamma_v\Gamma_{v'}}$ corresponds to the effective parameters to be determined by fitting experimental line positions, and the $T_{\{s\}\{s'\}}^{\Omega(K,n\Gamma)\Gamma_v\Gamma_{v'}}$ are vibration-rotation operators defined as:

$$T_{\{s\}\{s'\}}^{\Omega(K,n\Gamma)\Gamma_v\Gamma_{v'}} = \beta \left[{}^{\varepsilon}V_{\{s\}\{s'\}}^{\Gamma_v\Gamma_{v'}(\Gamma)} \otimes R^{\Omega(K,n\Gamma)} \right]^{(A_1)}$$

Equation 12

where β is a numerical factor equal to $\sqrt{\Gamma_v}\left(-\sqrt{\Gamma_v}/4\right)^{\Omega/2}$ if $(K, n\Gamma) = (0, A_1)$, and equal to 1 otherwise. As shown in Equation 12 the vibration-rotation operators $T_{\{s\}\{s'\}}^{\Omega(K,n\Gamma)\Gamma_v\Gamma_{v'}}$ are obtained by the totally symmetric coupling of a vibrational operator, ${}^{\varepsilon}V_{\{s\}\{s'\}}^{\Gamma_v\Gamma_{v'}(\Gamma)}$, and rotational operator $R^{\Omega(K,n\Gamma)}$.

The coupling scheme used in the STDS software [45] is described in ref. [44]. The vibrational operator ${}^{\varepsilon}V_{\{s\}\{s'\}}^{\Gamma_v\Gamma_{v'}(\Gamma)}$ is generated by recursive coupling of the creation (a$^+$) and annihilation (a) elementary operators for each normal mode. ε= ±1, is the parity under time reversal. Rotational operators, $R^{\Omega(K,n\Gamma)}$, are also built recursively from successive couplings of the elementary tensor R$^{1(1)}$ = 2**J** using the method of Moret-Bailly [46,47] and Zhilinskii [48]. They are symmetrised using the $O(3) \supset T_d$ orientation matrix defined in ref. [49] and [50]. Ω is the degree in J_α operators. The order of each individual term in Equation 12 is defined as:

$$\mathcal{O}_H = \Omega + \Omega_v - 2$$

Equation 13

Where Ω and Ω_v are the order of rotational and vibrational operators respectively.

Thus, the vibration-rotation Hamiltonian can be written as sum of individual contributions of polyads within a certain limit of energy, which is considered up to the Tetradecad (P$_4$) in this work:

$$\widetilde{H}^{\langle Tetradecad \rangle} = \widetilde{H}_{\{P_0\}}^{\langle P_4 \rangle} + \widetilde{H}_{\{P_1\}}^{\langle P_4 \rangle} + \widetilde{H}_{\{P_2\}}^{\langle P_4 \rangle} + \widetilde{H}_{\{P_3\}}^{\langle P_4 \rangle} + \widetilde{H}_{\{P_4\}}^{\langle P_4 \rangle}$$

Equation 14

6.1 Effective parameters

The effective vibration-rotation Hamiltonian of methane described above, was built using successive global analyses of infrared absorption and Raman scattering spectra up to and including the Tetradecad (6200 cm^{-1}).

The word "global" refers here to the simultaneous account of all polyads within a certain limit of energy. Thereby, the resulting effective parameters are valid for all considered polyads, unlike the band by band analyses which focuses only on a given polyad.

The main global analyses achieved in this context are published by S. Albert et al. [51] and L. Daumont et al. [52] including the GS, Dyad, Pentad and the Octad systems. This work was updated later by including new assignments in the Tetradecad absorption band by A. Nikitin et al. [53]. A total of 19,751 infrared and Raman transitions were used in these works. They involve essentially lines from the cold bands and the first related hot bands: (P1 -P1) and (P2 -P2) in the far infrared region, and the (P2 - P1) and (P3 - P1) hot bands. Such data are obtained at low or moderate temperature and thus are rotationally limited, typically up to J = 20. Let us also mention recent line-by-line analyses reported by Nikitin et al. in the octad and tetradecad regions [54–58].

The same spectral regions were reinvestigated recently in Dijon using high temperature emission spectra recorded by R. Georges and coworkers at SOLEIL Synchrotron and in Rennes, typically up to 1500 K see Refs. [24,59,60]. As resulted from these works, the number of assigned transitions was extended to 39,614 vibration-rotation. They involve highly rotational states up to J = 30 of the Dyad and the Pentad cold band systems and their related hot bands. New weak hot bands were also identified and thus a significant improvement of the effective vibration-rotation parameters was achieved. They are provided in reference [24] as supplementary material. The Dijon assigned line list is summarized in Table 4.

Table 4: Summary of vibration-rotation transitions of methane $^{12}CH_4$ included in the global analysis [2].

Transition $P_{n'}$ - $P_{n''}$	Region cm^{-1}		# data	J''_{min}	J''_{max}	d$_{RMS}$ 10^{-3} cm^{-1}	Ref.
$P_0 - P_0$	0.008 -	2506.481	135	2	19	102.625 (kHz for Q branch) 0.143 (R branch)	[53,61,62]
$P_1 - P_0$	1023.275 -	1778.830	2224	0	30	2.832	[53,59]
$P_2 - P_0$	2207.366 -	3274.188	5876	0	30	3.946	[24,53,63]
$P_3 - P_0$	3518.877 -	4746.620	7907	0	18	5.948	[53]
$P_4 - P_0$	4885.723 -	6204.613	3009	0	14	23.225	[53]
$P_1 - P_1$	13.402 -	2532.357	124	1	14	148.717 (kHz for Q branch) 0.180 (R branch)	[53,61,62]
$P_2 - P_1$	1100.443 -	1930.376	5272	0	29	4.523	[53,59]
$P_3 - P_1$	2334.157 -	3298.380	4932	0	27	8.392	[24,53]
$P_2 - P_2$	6.895 -	17.391	16	4	12	178.142 (kHz for Q branch)	[53]
$P_3 - P_2$	1102.505 -	1426.872	6454	0	28	6.579	[53,59]
$P_4 - P_2$	2822.352 -	3175.063	1525	1	20	11.759	[24]
$P_4 - P_3$	1129.633 -	1382.236	2140	1	21	6.518	[59]

6.2 Calculation of Raman intensities

The theoretical background of Raman intensity calculation using tensorial formalism as for the effective Hamiltonian is detailed in Refs. [25,38]. It will be described briefly in this section.

The Raman intensity strength between two states i and f is given in a similar way to that of the absorption or emission line strengths:

$$I_{if} = R_{if} g_i e^{-hcE_i/kT} \sum_{\Gamma,\Gamma'} \sum_{M_i,M_f} \left| < \tilde{\varphi}_i |\tilde{\alpha}_{\Gamma\Gamma'}| \tilde{\varphi}_f > \right|^2$$

Equation 15

where R_{if} is a constant depending on the experimental conditions, g_i is the nuclear spin statistical weight of the state of energy E_i equal to 5, 2 and 3 for A, E and F symmetries, respectively. $\tilde{\alpha}_{\Gamma\Gamma'}$ is the polarizability tensor. The summation over Γ and Γ' depends on the experimental conditions i.e. the direction of the observation of the scattered light and the polarization of the pump and of the probe beam. $\tilde{\varphi}_{i;f}$ corresponds to the effective eigenfunctions of E_i and E_f states respectively. Effective polarizability parameters were taken from the study of

Jourdanneau et al. [38] who expanded the polarizability operator up to order two. No parameters were fitted here concerning the Heff nor the polarizability tensor.

The Equation 15 can be separated in two contributions: the isotropic ($\mathcal{P}_{if}$) and anisotropic ($\mathcal{A}_{if}$) parts of the polarizability:

$$I_{if} = g_i e^{-\frac{hcE_i}{kT}} (2J_i + 1)(2J_f + 1)\left(S_0 \left|\mathcal{P}_{if}^2\right| + S_2 \left|\mathcal{A}_{if}^2\right|\right)$$

Equation 16

where S_l are the Stone coefficients which depend on the conditions of observation, see for example Appendix A of Ref. [38]. They are expressed as:

$$S_0 = \sum_{\Gamma,\Gamma'} \left|< 0; 0 |\Gamma\Gamma' >\right|^2$$

Equation 17

$$S_2 = \frac{1}{5} \sum_{M,\Gamma,\Gamma'} \left|< 2; M |\Gamma\Gamma' >\right|^2$$

Equation 18

According to Ref.[38] three cases are distinguished in the case of spontaneous Raman scattering:

- Parallel polarization of the probe beam and the pump beam (‖): $S_0 = \frac{1}{3}$ and $S_2 = \frac{2}{15}$
- Perpendicular polarization of the probe beam and the pump beam (⊥): $S_0 = 0$ and $S_2 = \frac{1}{10}$
- Spontaneous Raman scattering without a polarizer : $S_0 = \frac{1}{3}$ and $S_2 = \frac{7}{30}$

6.3 Calculation of the Voigt lineshape

The Voigt line profile ($\mathcal{V}$) is a convolution of the Lorentzian ($\mathcal{L}$) and Gaussian ($\mathcal{G}$) lineshape functions, given by Equation 19:

$$\mathcal{V}(\lambda, \sigma, \gamma) = \mathcal{G}(\lambda, \sigma) * \mathcal{L}(\lambda, \gamma)$$

Equation 19

We apply a commonly used method to evaluate the Voigt profile, described in [64], shown in Equation 20:

$$\mathcal{V}(\lambda, \sigma, \gamma) = \frac{1}{\sigma\sqrt{2\pi}} Re\left[\mathcal{W}\left(\frac{v_0 - \lambda + i\gamma}{\sigma\sqrt{2}}\right)\right]$$

Equation 20

Where $Re[\mathcal{W}(z)]$ is the real part of the Faddeeva function, v_0 is the wavelength of the spectral line, λ is the wavelength at which the relative line intensity is being calculated, σ is the standard deviation of the Gaussian line broadening, and γ the half-width at half maximum of the Lorentzian line broadening.

7. Acknowledgments

8. Citations

[1]   Haller TW, Reising HH, Clemens NT, Varghese PL. High-Pressure Spontaneous Raman Scattering Based Temperature Measurements 2017:1–8. doi:10.2514/6.2017-3898.

[2]   Lo A, Cléon G, Vervisch P, Cessou A. Spontaneous Raman scattering: A useful tool for investigating the afterglow of nanosecond scale discharges in air. Appl Phys B Lasers Opt 2012;107:229–42. doi:10.1007/s00340-012-4874-3.

[3]   Lempert WR, Adamovich I V. Coherent anti-Stokes Raman scattering and spontaneous Raman scattering diagnostics of nonequilibrium plasmas and flows. J Phys D Appl Phys 2014. doi:10.1088/0022-3727/47/43/433001.

[4]   den Harder N, van den Bekerom DCM, Al RS, Graswinckel MF, Palomares JM, Peeters FJJ, et al. Homogeneous CO_2 conversion by microwave plasma: Wave propagation and diagnostics. Plasma Process Polym 2017. doi:10.1002/ppap.201600120.

[5]   Minea T, van den Bekerom DCM, Peeters FJJ, Zoethout E, Graswinckel MF, van de Sanden MCM, et al. Non-oxidative methane coupling to C2hydrocarbons in a microwave plasma reactor. Plasma Process Polym 2018. doi:10.1002/ppap.201800087.

[6]   Kozàk T, Bogaerts A. Splitting of CO2by vibrational excitation in non-equilibrium plasmas: A reaction kinetics model. Plasma Sources Sci Technol 2014. doi:10.1088/0963-0252/23/4/045004.

[7]   Snoeckx R, Bogaerts A. Plasma technology-a novel solution for CO2conversion? Chem Soc Rev 2017. doi:10.1039/c6cs00066e.

[8]   Patil BS, Wang Q, Hessel V, Lang J. Plasma N2-fixation: 1900–2014. Catal Today 2015. doi:10.1016/j.cattod.2015.05.005.

[9]   Butterworth T, Elder R, Allen R. Effects of particle size on CO2reduction and discharge characteristics in a packed bed plasma reactor. Chem Eng J 2016. doi:10.1016/j.cej.2016.02.047.

[10]   Gatti N, Ponduri S, Peeters FJJ, Van Den Bekerom DCM, Minea T, Tosi P, et al. Preferential vibrational excitation in microwave nitrogen plasma assessed by Raman scattering. Plasma Sources Sci Technol 2018. doi:10.1088/1361-6595/aabd60.

[11]   Klarenaar BLM, Engeln R, Van Den Bekerom DCM, Van De Sanden MCM, Morillo-Candas AS, Guaitella O. Time evolution of vibrational temperatures in a CO<inf>2</inf>glow discharge measured with infrared absorption spectroscopy. Plasma Sources Sci Technol 2017. doi:10.1088/1361-6595/aa902e.

[12]   Fridman A. Plasma Chemistry. 2008. doi:10.1017/CBO9780511546075.

[13]   Mehta P, Barboun P, Herrera FA, Kim J, Rumbach P, Go DB, et al. Overcoming ammonia synthesis scaling relations with plasma-enabled catalysis. Nat Catal 2018. doi:10.1038/s41929-018-0045-1.

[14]   Fincke JR, Anderson RP, Hyde T, Detering BA, Wright R, Bewley RL, et al. Plasma Thermal Conversion of Methane to Acetylene. Plasma Chem Plasma Process 2002;22.

[15]   Rusanov AVD, Babaritskii AI, Baranov IE, Bibikov MB, Deminskii MA, Demkin SA, et al. V.D. Rusanov 2003 - Non equilibrium effect of atm pressure mw discharge plasma on methane 2004;395:637–40.

[16]   Bekerom D van den. Vibrational excitation for efficient chemistry in microwave plasmas. TU/e, 2018.

[17]   Rusanov VD, Fridman A a., Sholin GV. The physics of a chemically active plasma with nonequilibrium vibrational excitation of molecules. Uspekhi Fiz Nauk 1981;134:185. doi:10.3367/UFNr.0134.198106a.0185.

[18]   Treanor CE, Rich JW, Rehm RG. Vibrational Relaxation of Anharmonic Oscillators with Exchange-Dominated Collisions. J Chem Phys 1968. doi:10.1063/1.1668914.

[19]   Vasconcelos MHC. Vibrational Relaxation Times in Methane: The Optic-Acoustic Effect. Technical University of Eindhoven, 1976.

[20]   Brehmer F, Welzel S, Klarenaar BLM, Van Der Meiden HJ, Van De Sanden MCM, Engeln R. Gas temperature in transient CO2 plasma measured by Raman scattering. J Phys D Appl Phys 2015. doi:10.1088/0022-3727/48/15/155201.

[21]   Robiette AG, Mills IM. Intensity perturbations due to v3 v4 Coriolis interaction in methane. J Mol Spectrosc 1979. doi:10.1016/0022-2852(79)90195-4.

[22]   Gray DL, Robiette AG. The anharmonic force field and equilibrium structure of methane. Mol Phys 1979. doi:10.1080/00268977900101401.

[23]   Wenger C, Boudon V, Rotger M, Sanzharov M, Champion JP. XTDS and SPVIEW: Graphical tools for the analysis and simulation of high-resolution molecular spectra. J Mol Spectrosc 2008;251:102–13. doi:10.1016/j.jms.2008.01.011.

[24] Amyay B, Gardez A, Georges R, Biennier L, Vander Auwera J, Richard C, et al. New investigation of the v_3 C-H stretching region of $^{12}CH_4$ through the analysis of high temperature infrared emission spectra. J Chem Phys 2018. doi:10.1063/1.5023331.

[25] Boudon V, Champion J, Gabard T, Loëte M, Rotger M, Wenger C. Spherical Top Theory and Molecular Spectra. Handb. high-resolution Mol. Spectrosc., John Wiley & Sons; 2011.

[26] Vasconcelos MHC de. Vibrational Relaxation Times in Methane the Optic-Acoustic Effect 1976.

[27] Boursier C, Ménard J, Doyennette L, Menard-Bourcin F. Rovibrational relaxation of methane in CH4-N2 mixtures: Time-resolved IR-IR double-resonance measurements at 193 K and kinetic modeling. J Phys Chem A 2003;107:5280–90. doi:10.1021/jp034265m.

[28] Herzberg G. Molecular Spectra and Molecular Structure II. Infrared and Raman Spectra of Polyatomic Molecules. 1991.

[29] Newville M, Ingargiola A, Stensitzki T, Allen DB. LMFIT: Non-Linear Least-Square Minimization and Curve-Fitting for Python. Zenodo 2014. doi:10.5281/ZENODO.11813.

[30] Magnotti G, Utsav KC, Varghese PL, Barlow RS. Raman spectra of methane, ethylene, ethane, dimethyl ether, formaldehyde and propane for combustion applications. J Quant Spectrosc Radiat Transf 2015;163:80–101. doi:10.1016/j.jqsrt.2015.04.018.

[31] Bevington PR, Robinson DK, Blair JM, Mallinckrodt AJ, McKay S. Data Reduction and Error Analysis for the Physical Sciences. Comput Phys 1993;7:415. doi:10.1063/1.4823194.

[32] Maroni P, Papageorgopoulos DC, Sacchi M, Dang TT, Beck RD, Rizzo TR. State-resolved gas-surface reactivity of methane in the symmetric C-H stretch vibration on Ni(100). Phys Rev Lett 2005. doi:10.1103/PhysRevLett.94.246104.

[33] Beck RD, Maroni P, Papageorgopoulos DC, Dang TT, Schmid MP, Rizzo TR. Vibrational mode-specific reaction of methane on a nickel surface. Science (80-) 2003. doi:10.1126/science.1088996.

[34] Juurlink LBF, Killelea DR, Utz AL. State-resolved probes of methane dissociation dynamics. Prog Surf Sci 2009;84:69–134. doi:10.1016/j.progsurf.2009.01.001.

[35] Nozaki T, Muto N, Kadio S, Okazaki K. Dissociation of vibrationally excited methane on Ni catalyst: Part 2. Process diagnostics by emission spectroscopy. Catal Today 2004;89:67–74. doi:10.1016/j.cattod.2003.11.039.

[36] Kim J, Abbott MS, Go DB, Hicks JC. Enhancing C-H Bond Activation of Methane via Temperature-Controlled, Catalyst-Plasma Interactions. ACS Energy Lett 2016. doi:10.1021/acsenergylett.6b00051.

[37] Zhao H, Ladommatos N. Optical diagnostics for in-cylinder mixture formation measurements in IC engines. Prog Energy Combust Sci 1998. doi:10.1016/S0360-1285(98)80026-9.

[38] Jourdanneau E, Chaussard F, Saint-Loup R, Gabard T, Berger H. The methane Raman spectrum from 1200 to 5500 cm-1: A first step toward temperature diagnostic using methane as a probe molecule in combustion systems. J Mol Spectrosc 2005;233:219–30. doi:10.1016/j.jms.2005.07.004.

[39] Kiefer J, Seeger T, Steuer S, Schorsch S, Weikl MC, Leipertz A. Design and characterization of a Raman-scattering-based sensor system for temporally resolved gas analysis and its application in a gas turbine power plant. Meas Sci Technol 2008. doi:10.1088/0957-0233/19/8/085408.

[40] P.B.Kelly, S.G.Westre. Resonance Raman spectroscopy of the methyl radical. Chem Phys Lett 1988;151:253–7.

[41] Pacansky J, Koch W, Miller MD. Analysis of the Structures, Infrared Spectra, and Raman Spectra for the Methyl, Ethyl, Isopropyl, and tert-Butyl Radicals. J Am Chem Soc 1991;113:317–28. doi:10.1021/ja00001a046.

[42] Van Helvoort K, Knippers W, Fantoni R, Stolte S. The Raman spectrum of ethane from 600 to 6500 cm-1 stokes shifts. Chem Phys 1987;111:445–65. doi:10.1016/0301-0104(87)85092-9.

[43] Song M-Y, Yoon J-S, Cho H, Itikawa Y, Karwasz GP, Kokoouline V, et al. Cross Sections for Electron Collisions with Methane. J Phys Chem Ref Data 2015;44:023101. doi:10.1063/1.4918630.

[44] Champion J, Loëte M, Pierre G. Spherical Top Spectra. Spectrosc. Earth's Atmos. Interstellar Mediu., Academic Press; 1992, p. 339–422.

[45] Wenger C, Champion JP. Spherical Top Data System (STDS) software for the simulation of spherical top spectra. J Quant Spectrosc Radiat Transf 1998. doi:10.1016/S0022-4073(97)00106-4.

[46] Moret-Bailly J. Calculation of the frequencies of the lines in a threefold degenerate fundamental band of a spherical top molecule. J Mol Spectrosc 1965. doi:10.1016/0022-2852(65)90150-5.

[47] Moret-Bailly J. Sur l'interpretation des spectres de vibration-rotation des molecules a symetrie tetraedrique ou octaedrique. Cah Phys 1961;15.

[48] Zhilinski´ı B. Reduction of rotational operators to standard form. J Mol Spectrosc 1981.

[49] Champion J, Pierre G, Michelot F, Moret-Bailly J. Composantes cubiques normales des tenseurs spheriques. Can J Phys 1977;55:512–20.

[50] Rey M, Boudon V, Wenger C, Pierre G, Sartakov B. Orientation of O(3) and SU(2) $\otimes$ C$_I$ representations in cubic point groups (O$_h$, T$_d$) for application to molecular spectroscopy. J Mol Spectrosc 2003. doi:10.1016/S0022-2852(03)00056-0.

[51] Albert S, Bauerecker S, Boudon V, Brown LR, Champion J-P, Loëte M, et al. Global analysis of the high resolution infrared spectrum of methane 12CH4 in the region from 0 to 4800cm−1. Chem Phys 2009. doi:10.1016/j.chemphys.2008.10.019.

[52] Daumont L, Nikitin A V., Thomas X, Régalia L, Von der Heyden P, Tyuterev VG, et al. New assignments in the 2μm transparency window of the12CH4Octad band system. J Quant Spectrosc Radiat Transf 2013. doi:10.1016/j.jqsrt.2012.08.025.

[53] Nikitin A V., Boudon V, Wenger C, Albert S, Brown LR, Bauerecker S, et al. High resolution spectroscopy and the first global analysis of the Tetradecad region of methane 12CH4. Phys Chem Chem Phys 2013. doi:10.1039/c3cp50799h.

[54] Nikitin A V., Lyulin OM, Mikhailenko SN, Perevalov VI, Filippov NN, Grigoriev IM, et al. GOSAT-2014 methane spectral line list. J Quant Spectrosc Radiat Transf 2015. doi:10.1016/j.jqsrt.2014.12.003.

[55] Nikitin A V., Thomas X, Daumont L, Rey M, Sung K, Toon GC, et al. Assignment and modelling of 12 CH 4 spectra in the 5550–5695, 5718–5725 and 5792–5814 cm −1 regions. J Quant Spectrosc Radiat Transf 2018. doi:10.1016/j.jqsrt.2018.08.006.

[56] Nikitin AV, Thomas X, Daumont L, Rey M, Sung K, Toon GC, et al. Measurements and modeling of long-path ^{12}CH$_4$ spectra in the 5300–5550 cm^{-1} region. J Quant Spectrosc Radiat Transf 2017. doi:10.1016/j.jqsrt.2017.07.030.

[57] Nikitin A V., Chizhmakova IS, Rey M, Tashkun SA, Kassi S, Mondelain D, et al. Analysis of the absorption spectrum of 12CH4 in the region 5855–6250 cm−1 of the 2v3 band. J Quant Spectrosc Radiat Transf 2017. doi:10.1016/j.jqsrt.2017.05.014.

[58] Nikitin A V., Thomas X, Régalia L, Daumont L, Rey M, Tashkun SA, et al. Measurements and modeling of long-path 12CH4 spectra in the 4800-5300cm-1 region. J Quant Spectrosc Radiat Transf 2014. doi:10.1016/j.jqsrt.2014.02.005.

[59] Amyay B, Louviot M, Pirali O, Georges R, Vander Auwera J, Boudon V. No Global analysis of the high temperature infrared emission spectrum of 12CH4 in the dyad (V2/V4) region. J Chem Phys 2016;144.

[60] Amyay B, Boudon V. Vibration-rotation energy levels and corresponding eigenfunctions of 12CH4 up to the Tetradecad. J Quant Spectrosc Radiat Transf 2018.

[61] Boudon V, Pirali O, Roy P, Brubach JB, Manceron L, Vander Auwera J. The high-resolution far-infrared spectrum of methane at the SOLEIL synchrotron. J Quant Spectrosc Radiat Transf 2010. doi:10.1016/j.jqsrt.2010.02.006.

[62] Bray C, Cuisset A, Hindle F, Mouret G, Bocquet R, Boudon V. Spectral lines of methane measured up to 2.6 THz at sub-MHz accuracy with a CW-THz photomixing spectrometer: Line positions of rotational transitions induced by centrifugal distortion. J Quant Spectrosc Radiat Transf 2017. doi:10.1016/j.jqsrt.2017.04.010.

[63] Abe M, Iwakuni K, Okubo S, Sasada H. Accurate transition frequency list of the 3 band of methane from sub- Doppler resolution comb-referenced spectroscopy. J Opt Soc Am B 2013;30:1027–35.

[64] Hill C. Learning Scientific Programming with Python. 2016. doi:10.1017/cbo9781139871754.